Inorganic Chemistry

Article

pubs.acs.org/IC

# Low-Temperature Vaterite-Type $LuBO_3$, a Vacancy-Stabilized Phase Synthesized at High Temperature

Zhi-Jun Zhang,[†] Teng-Teng Jin,[‡] Meng-Meng Xu,[§] Qing-Zhen Huang,[∥] Man-Rong Li,[⊥] and Jing-Tai Zhao*[,†]

[†]School of Materials Science and Engineering, Shanghai University, Shanghai 200072, P. R. China

[‡]SGS-CSTC Standards Technical Services, 889 Yishan Road, Shanghai, P. R. China

[§]Key Laboratory of Transparent Opto-Functional Inorganic Materials of Chinese Academy of Sciences, Shanghai Institute of Ceramics, Shanghai 200050, P. R. China

[∥]NIST Center for Neutron Research, National Institute of Standards and Technology (NIST), Gaithersburg, Maryland 20899, United States

[⊥]Department of Chemistry and Chemical Biology, Rutgers, The State University of New Jersey, Piscataway, New Jersey 08854 United States

Ⓢ *Supporting Information*

**ABSTRACT:** Low-temperature vaterite-type $LuBO_3$ (π-LBO) was prepared by a solid-state reaction method at high temperature. The reasoning of the existence of vacancy-stabilized π-LBO was investigated for the first time using neutron diffraction patterns, Fourier transform infrared (FT-IR) spectra, and high-resolution transmission electron microscopy. The results clearly demonstrated that the B and O vacancies in π-LBO came into being during the heating process. The existence of an open $B_3O_9$ ring consisting of $BO_3$ and $BO_4$ units in π-LBO due to the B and O vacancies was demonstrated by FT-IR. The vacuum ultraviolet–ultraviolet spectroscopic properties of π-LBO were studied in detail. In addition, the luminescence mechanism of $Ce^{3+}$ in π-LBO was put forward and discussed with that of calcite-type $LuBO_3$ (β-LBO).

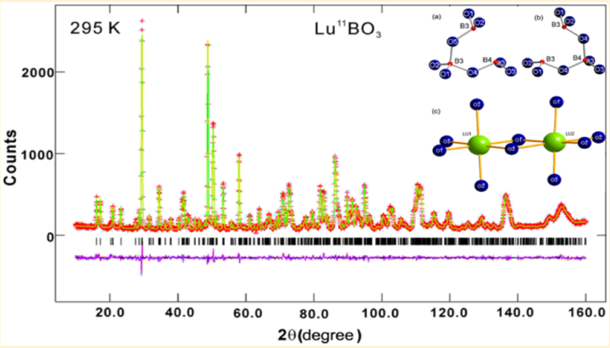

## 1. INTRODUCTION

Over the past decades, the rare-earth (RE) orthoborates $REBO_3$ have attracted tremendous attention because of their extraordinary optical properties, such as excellent damage threshold, high vacuum ultraviolet transparency, and high luminescent efficiency of $Ce^{3+}$ (or $Eu^{3+}$).[1,2] It is notable that $LuBO_3:Ce^{3+}$ with calcite type (i.e., β-LBO:$Ce^{3+}$) is the most famous orthoborate as a scintillator, which has been widely investigated during the past decade. The light yield of a calcite-type β-LBO:$Ce^{3+}$ polycrystallite is about 3 and 135 times that of commercial scintillators $Bi_4Ge_3O_{12}$ (BGO) and $PbWO_4$ (PWO), respectively. In addition, it exhibits several excellent properties such as fast decay (about 33 ns) and nonhygroscopy, etc.[3] Therefore, single crystals of β-LBO:$Ce^{3+}$ doped with Sc were successfully grown by Hatamoto et al. in 2011 using the Czochralski method.[4,5] Unfortunately, its overall light yield drops to less than 60% of BGO after doping with Sc. However, it is very difficult to grow pure β-LBO (calcite-type) single crystals because of the phase transition between calcite (β-LBO), low-temperature vaterite (π-LBO), and high-temperature vaterite (μ-LBO) phases. The true structures of π- and β-LBO, as well as the origin of their phase transitions, have long been a subject of interest and controversy.

There are few reports about the phase transitions of LBO. As early as 1961, the phase transition of $LuBO_3$ was first observed using high-temperature X-ray diffraction (XRD) and thermal analysis.[6] After that, Ren et al. investigated the crystal structure of high-temperature vaterite μ-LBO and reported that the observed high-temperature vaterite μ-LBO was isostructural with the hexagonal structure of $YbBO_3$ with space group $P6_322$ (No. 182).[7] Furthermore, the temperature dependence of Raman spectroscopy was used to investigate the phase transition in $LuBO_3$.[7] It was believed that the phase transition between π- and β-LBO is related to the broken bond of one B–O in the cyclic $B_3O_9$ rings at high temperature, leading to an open $B_3O_9$ ring consisting of $BO_3$ and $BO_4$ units. However, the origin of the phase transitions and the true crystal structures of $LuBO_3$ have not been studied to date. Thus, a clear

**Special Issue:** To Honor the Memory of Prof. John D. Corbett

**Received:** September 27, 2014
**Published:** January 9, 2015

DOI: 10.1021/ic502337x
*Inorg. Chem.* 2015, 54, 969–975

understanding of the true crystal structures and the phase transitions between different $LuBO_3$ phases not only opens a new avenue for growing large β-LBO single crystals with high performance as scintillators but also provides some new insights for an in-depth understanding of the luminescence mechanism. Generally, XRD, Fourier transform infrared (FT-IR), and Raman techniques are used to characterize the crystal structures of $REBO_3$. The recent high-resolution luminescence spectra were applied to study the features of cations[7,8] but revealed a difficulty in unambiguously distinguishing between the alternatives of having either two or three cation sites in the structure. Thus, the neutron powder diffraction as a complementary structure solution tool was used to clarify the structures of $LuBO_3$ because the coherent elastic scattering lengths of rare earth, oxygen, and boron are of the same order of magnitude [$b_c(\mathrm{Lu}) = 7.21$ fm, $b_c(^{11}\mathrm{B}) = 6.65$ fm, and $b_c(\mathrm{O}) = 5.803$ fm]. The problem of the high absorption of neutrons by boron was overcome by using the $^{11}B$ isotope. Herein, we put forward the reasoning of the existence of low-temperature vaterite π-LBO for the first time, using neutron diffraction patterns, FT-IR spectra, and HRTEM. Moreover, the luminescence properties of $Ce^{3+}$ in these two phases have also been investigated based on their crystal structures.

## 2. EXPERIMENTAL SECTION

**2.1. Synthesis of Undoped $LuBO_3$ and Rare-Earth-Doped $LuBO_3$.** The polycrystalline undoped $LuBO_3$, $Lu^{11}BO_3$, and $Ce^{3+}$-doped $LuBO_3$ samples were prepared by a solid-state reaction method. The starting materials were $Lu_2O_3$ (Aldrich, 99.999%), $H_3BO_3$ (Aldrich, 99.99%), $H_3{}^{11}BO_3$ (Aldrich, 99.99%), and $CeO_2$ (Aldrich, 99.999%). Suitable amounts of raw materials were weighed out and subsequently mixed and ground together in an agate mortar. The powder mixtures were then transferred into a platinum crucible with a cover. Subsequently, those powder mixtures were fired at 1200 °C for 24 h in a chamber furnace in air. After firing, the samples were gradually cooled to room temperature in the furnace. There was no apparent reaction of the products with the platinum crucibles. However, it is difficult to obtain a single phase of π- and β- LBO when using stoichiometric amounts of $Lu_2O_3$ and $H_3BO_3$ ($H_3{}^{11}BO_3$) because of evaporation of $B_2O_3$ at high temperature. Thus, 10% excess of $H_3BO_3$ ($H_3{}^{11}BO_3$) was used for the preparation of a single phase to compensate for evaporation of $B_2O_3$. For a high-pressure test, β-LBO was heated at 1250 and 1350 °C under 6 GPa for 30 min in a Walker-type Multi Anvil Press and then quenched to room temperature by turning off the voltage supply to the resistance furnace, which reduced the temperature to room temperature in a few seconds. The pressure was maintained during the temperature quenching and then released slowly. The concentration of the $Ce^{3+}$ activator is 1 mol % of $Lu^{3+}$ in π- and β-LBO.

**2.2. Sample Characterization.** The powder XRD data for phase identification were collected with a Rigaku D/max-2550 V diffractometer (Cu Kα, scanning rate = 2°/min at 40 kV and 50 mA). The neutron powder diffraction data were collected at the NIST with a copper monochromator ($\lambda = 1.5403$ Å) at room temperature. The lattice parameter was calculated by a combination of the Rietveld and Lebail methods in *GSAS*, and all structure refinements were performed using *GSAS* software. The morphology and selected-area electron diffraction (SAED) were investigated by using high-resolution transmission electron microscopy (HRTEM; JEOL200CX). FT-IR spectra were recorded with a Spectrum 100 (PerkinElmer) in a scanning range from 2000 to 400 $cm^{-1}$. The vacuum ultraviolet–ultraviolet (VUV-UV) excitation spectra and VUV excited emission spectra were measured at the VUV spectroscopy station of Beijing Synchrotron Radiation Facility, Institute of High Energy Physics, Chinese Academy of Sciences. The electron energy of the storage ring is 2.5 GeV, and the beam current is approximately from 160 to 60 mA in measurement. An ARC-VM-502-S monochromator (1200 g/mm) was used for the excitation spectra and an ARC SP-308 monochromator (1200 g/mm) for the emission spectra, and the signal was detected by a Hamamatsu H7421-50 photomultiplier. The pressure in the sample chamber was $2 \times 10^{-5}$ mbar. The resolution of the instruments was about 0.2 nm. The relative VUV-UV excitation intensities of the samples were corrected by comparing the measured excitation intensities of the samples with the excitation intensities of sodium salicylate ($o$-$HOC_6H_4COONa$) in the same excitation conditions. All of the luminescent spectra were recorded at room temperature. The transient decays were recorded on an Edinburgh Instruments (FLS920) spectrofluorimeter equipped with both continuous (450 W) and pulsed xenon lamps.

## 3. RESULTS AND DISCUSSION

**3.1. Crystal Structure of the Low-Temperature Vaterite π-LBO.** Figure 1 shows the powder XRD patterns of β-LBO, β-$L^{11}BO$, and β-LBO:$Ce^{3+}$ (1 mol %) prepared at 1200 °C for 24 h using 10% excess of $H_3BO_3$ ($H_3{}^{11}BO_3$). All of them are consistent with the standard β-LBO pattern (ICSD no. 16525), and no impurity was obtained. In addition, π-LBO, π-$L^{11}BO$, and π-LBO:$Ce^{3+}$ (1 mol %) prepared at 1500 °C for 5 h using a 10% excess of $H_3BO_3$ ($H_3{}^{11}BO_3$) were obtained as single-phase materials with π-$ErBO_3$ structure (ICSD no. 422094), as shown in Figure 2.

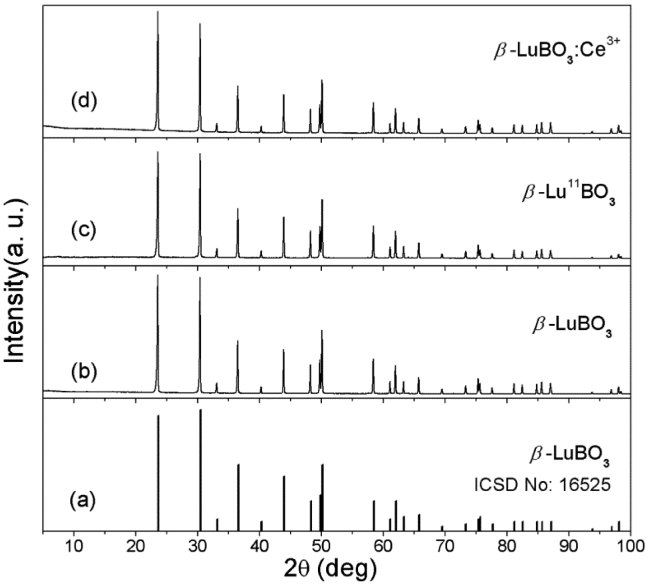

**Figure 1.** Powder XRD patterns of standard β-LBO (a), β-LBO prepared at 1200 °C for 24 h (b), β-$L^{11}BO$ prepared at 1200 °C for 24 h (c), and β-LBO:$Ce^{3+}$ (1 mol %) prepared at 1200 °C for 24 h (d).

Figure 3 exhibits the XRD patterns of β-LBO (Figure 1b) under high-pressure (6 GPa) and/or high-temperature post-treatments. Here high pressure was applied to β-LBO to check the possible phase transition from β- to π-LBO considering the smaller unit cell volume of the latter (see Table 2). It can be clearly seen that there is no phase transition of β-LBO under high pressure at room temperature probably because the energy barrier of the phase transition from β- to π-LBO is too high to overcome. However, when β-LBO was post-treated under high pressure (6 GPa) and high temperature (1250 and 1350 °C), it is worth noting that π-LBO, together with an unknown phase, appeared in the final product, indicating that part of β-LBO transforms into π-LBO. In order to investigate the real structure of π-LBO, neutron powder diffraction was applied on π-$L^{11}BO$,

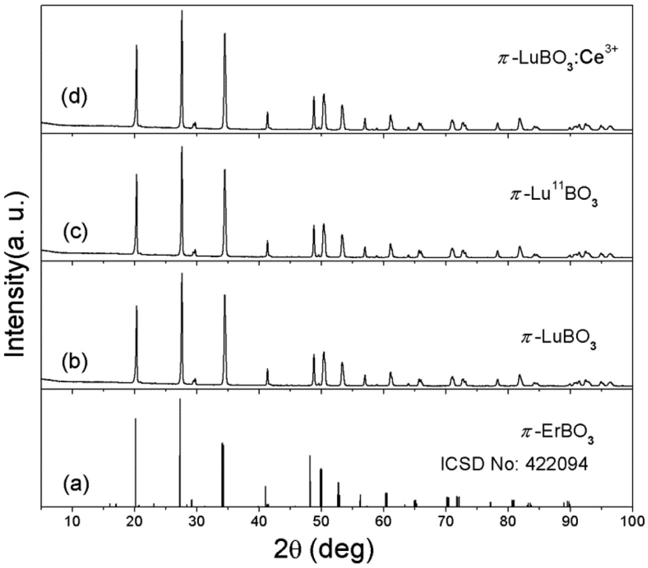

**Figure 2.** Powder XRD patterns of standard $\pi$-$ErBO_3$ (a), $\pi$-LBO prepared at 1500 °C for 5 h (b), $\pi$-$L^{11}BO$ prepared at 1500 °C for 5 h (c), and $\pi$-LBO:$Ce^{3+}$ (1 mol %) prepared at 1500 °C for 5 h (d).

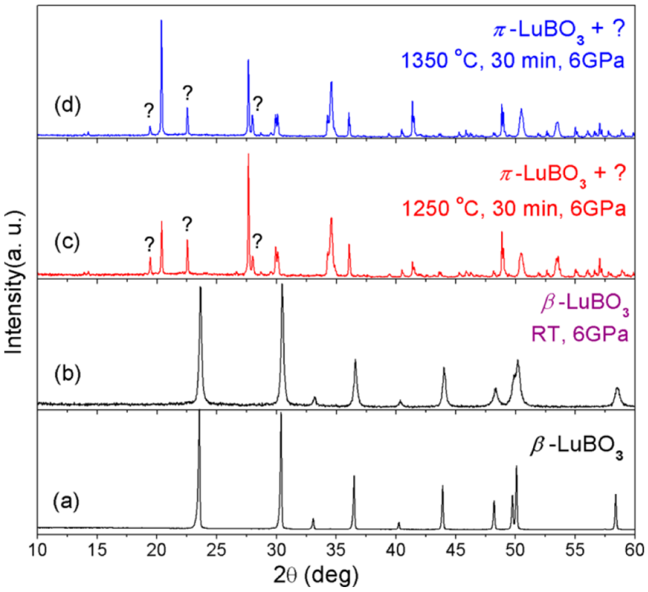

**Figure 3.** Powder XRD patterns of $\beta$-LBO prepared using a solid-state method at 1200 °C for 24 h (a), $\beta$-LBO post-treated under a pressure of 6 GPa at room temperature for 30 min (b), $\beta$-LBO post-treated under a pressure of 6 GPa and 1250 °C for 30 min (c), and $\beta$-LBO post-treated under a pressure of 6 GPa and 1350 °C for 30 min (d).

benefiting from the high absorption of neutrons by the $^{11}B$ isotope.

Figure 4 exhibits the refined neutron powder diffraction pattern of $\pi$-$L^{11}BO$ at room temperature. The index of the neutron powder diffraction pattern of $\pi$-$L^{11}BO$ using the Dicvol programs suggested monoclinic cells with parameters $a$ = 11.1733(4) Å, $b$ = 6.4612(2) Å, $c$ = 9.4628(3) Å, $\beta$ = 112.7632(15)°, and $V$ = 629.93(5) $Å^3$. The simulated neutron powder diffraction pattern using the atomic coordinates of $Y_{0.92}Sc_{0.08}BO_3$[9] was very similar to the experimental patterns; therefore, this structure model was used for subsequent calculations.[10] A pseudo-Voigt peak-shape function was used, and the absorption correction was applied on the basis of the experimentally measured transmission of the incident neutron beam through the sample. The details on data collection and structural refinements are tabulated in Table 1. The refined atomic coordinates and bond distances of $\pi$-$L^{11}BO$ are listed in Tables S1 and S2 in the Supporting Information (SI). Observed, calculated, and difference profiles for $\pi$-$L^{11}BO$ are shown in Figure 4.

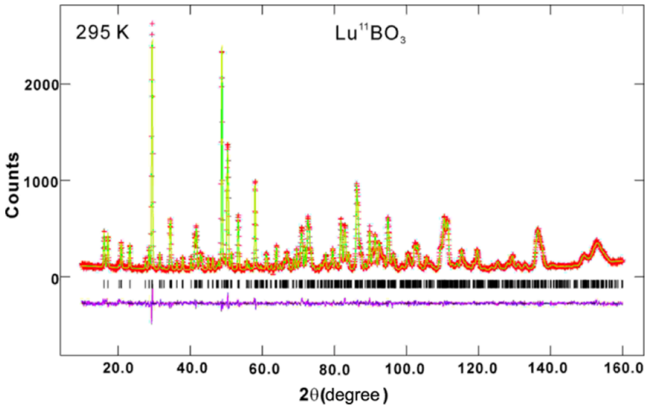

**Figure 4.** Refined neutron powder diffraction pattern of $\pi$-$Lu^{11}BO_3$ at room temperature. The observed data points, calculated profile, and difference curves are shown. The ticks correspond to the positions of the Bragg peaks.

**Table 1. Unit Cell Parameters and $R$ Factors of $\pi$-$L^{11}BO$ Obtained from Rietveld Refinement of the Neutron Powder Diffraction Data**

| | |
|---|---|
| formula | $Lu^{11}B_{0.929(9)}O_{2.93(1)}$ |
| fw (g/mol) | 221.94 |
| space group | monoclinic, $C2/c$ (No. 15) |
| $a$ (Å) | 11.173 (4) |
| $b$ (Å) | 6.461 (2) |
| $c$ (Å) | 9.462 (3) |
| $\beta$ (deg) | 112.7632(15) |
| volume ($Å^3$) | 629.93(5) |
| $Z$ | 12 |
| $\rho_{calc}$ ($g/cm^3$) | 7.343 |
| wavelength (Å) | 1.5403 |
| $2\theta$ range | $3.0 \leq 2\theta \leq 167.75$ |
| step size | 0.05° |
| goodness of fit ($\chi^2$) | 0.96 |
| $R_p$, $R_{wp}$ (%) | 5.44, 6.85 |

The low-temperature $\pi$-LBO phase crystallizes in the monoclinic system with a space group of $C2/c$, which is quite similar to that of $\pi$-$YBO_3$, $\pi$-$ErBO_3$, and $\pi$-$YbBO_3$.[9,11] It was supposed that the low-temperature phase $\pi$-LBO is isotypic to the typical vaterite-type $CaCO_3$. The misunderstanding of the crystal structure between $\pi$-LBO and vaterite-type $CaCO_3$ stems from their similar XRD patterns, originating from the relatively weak scattering of B, C, and bridged O atoms. However, the exact ordering of anions in the structures is difficult to discern. Figure 5a shows a projection of the crystal structure of the low-temperature phase LBO along the $b$ axis. The crystal structure could be described as an alternative stacking of borate layers and lutetium sheets. The B atoms are all tetrahedrally coordinated with four O atoms, leading to the formation of $BO_4$ units. In addition, three-membered borate $B_3O_9$ rings are further formed through sharing of the vertices of

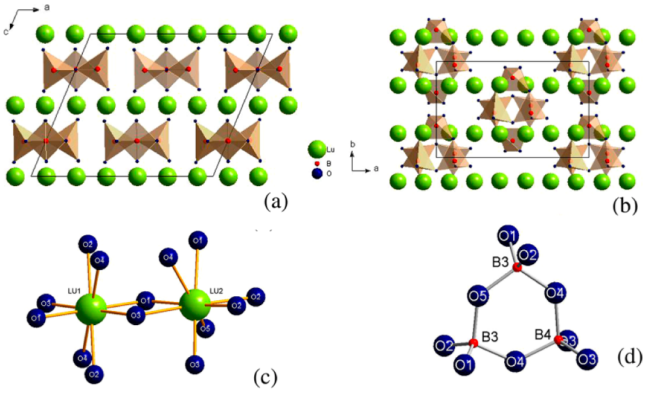

**Figure 5.** Projection of the crystal structure of $\pi$-LBO along the *b* (a) and *c* (b) axes. Coordination polyhedra of the Lu1 and Lu2 (c) and B (d) atoms.

two B(3)$O_4$ units and one B(4)$O_4$ unit (Figure 5d). The average B−O bond distances are in the range from 1.475(2) to 1.471(5) Å, which are similar to typical tetrahedral borate groups.[11] The $B_3O_9$ rings are stacked in a shifted arrangement viewed along the *c* axis. Earlier structure determinations assumed that the presence of rare-earth cations inside the $B_3O_9$ rings[12] can be completely ruled out according to the result of neutron diffraction. What is more, there are two different types of O atoms: one is the terminal O atom of the $BO_4$ units, including O1, O2, and O3, and the other is the bridged O atom of the $BO_4$ units, i.e., the vertices of the $B_3O_9$ rings, including O4 and O5. Figure 5b shows another view of the structure projected along the *c* axis. Meanwhile, the $Lu^{3+}$ ions are located in two different environments. As shown in Figure 5c, Lu1 (4c) and Lu2 (8f) are all coordinated with eight O atoms. The distances of the Lu−O bonds are in the typical range from 2.200(4) to 2.420(4) Å (Table S2 in the SI), which is consistent with those observed in $Lu_2WO_6$ [2.185(15)−2.489(15) Å][13] but smaller than those of the Er−O bonds [2.236(2)−2.446(2) Å] in $ErBO_3$[11] because of the smaller size of $Lu^{3+}$ than $Er^{3+}$.[14]

Surprisingly, it is observed that there are B and O vacancies in $\pi$-LBO according to the Rietveld refinement of the neutron diffraction pattern tabulated in Table S1 in the SI. The existence of B and O vacancies can be further demonstrated by TEM images. Figure 6 shows the SAED of $\pi$-LBO along $[\bar{2}33]$ (a) and $[1\bar{1}0]$ (b). The electron diffraction patterns can be easily indexed, and the monoclinic system of $\pi$-LBO can be validated. Moreover, parts c and d of Figure 6 show HRTEM images of the sample in Figure 6b and the corresponding inverse fast Fourier transform (FFT) pattern of the selected area marked by red rectangular lines. The stacking fault can be observed clearly in HRTEM images and its corresponding inverse FFT pattern. This interesting observation of the stacking fault is probably related to the existence of B and O vacancies in $\pi$-LBO.

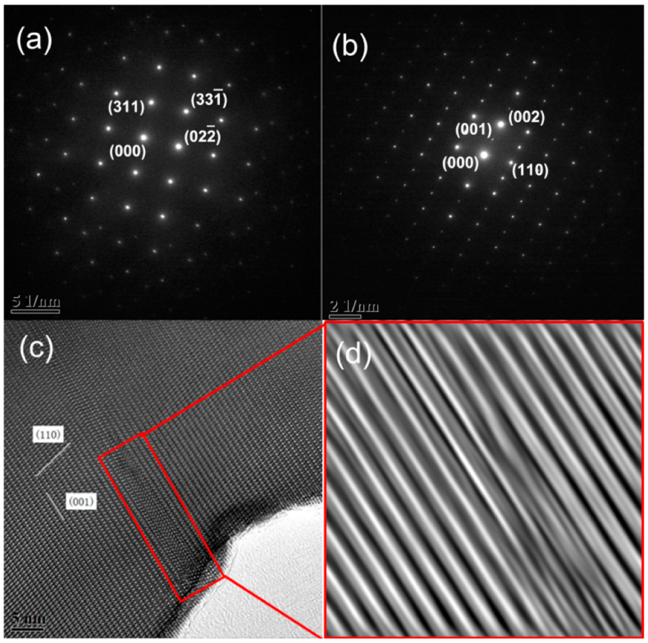

**Figure 6.** SAED of $\pi$-LBO along $[\bar{2}33]$ (a) and $[1\bar{1}0]$ (b). HRTEM images of the sample in part b (c). Corresponding inverse FFT pattern of the selected area marked by a white ellipse (d).

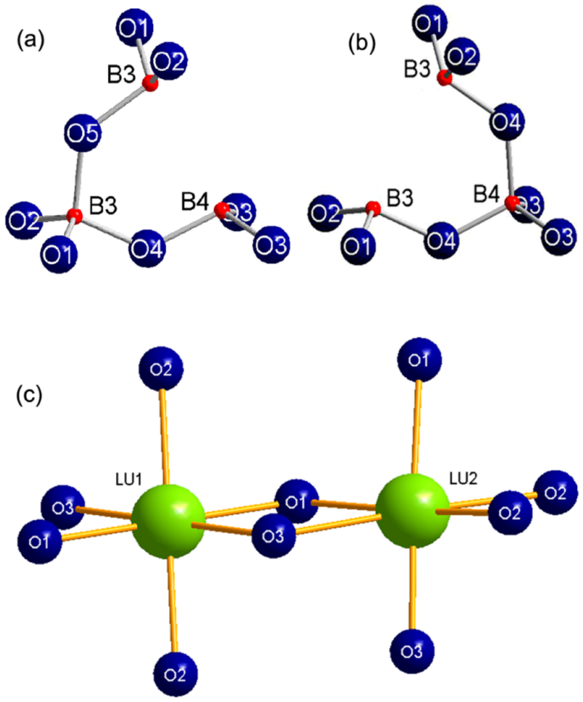

**Figure 7.** Coordination spheres of the B cations without one O4 or O5 (a and b) and Lu cations without one O4 or O5 (c).

All of the results above reveal that the existence of B and O vacancies in $\pi$-LBO will introduce the local structure aberration. Parts a and b of Figure 7 show the coordination environment of B atoms in the isolated open $B_3O_9$ rings lacking O4 or O5 atoms (bridging O atoms), resulting in $BO_3$ and $BO_4$ units, which is similar to the crystal structure of $\chi$-$DyBO_3$ stated by Huppertz et al.[15] In addition, two Lu cations in the structure are both 6-fold-coordinated and lacking O4 or O5 atoms (bridging O atoms), as shown in Figure 7c. In order to compare the crystal structures of $\pi$- and $\beta$-LBO, the crystal structure of $\beta$-LBO was refined from the neutron powder diffraction data. It was indexed in the trigonal unit cell with $R\bar{3}c$ symmetry and the parameters $a$ = 4.914 (13) Å, $c$ = 16.210 (7) Å, and $V$ = 339.059(2) Å$^3$. The Rietveld refinement fit of the neutron diffraction pattern and the crystallographic data of $\beta$-$L^{11}BO$ are shown in Figures S1 and S2 in the SI and Tables 2 and S3 in the SI.

**Table 2. Comparison of the Crystallographic Data between the π-L$^{11}$BO, β-L$^{11}$BO, and π-LBO Reported**

| | | | |
|---|---|---|---|
| empirical formula | Lu$^{11}$B$_{0.929(9)}$O$_{2.93(1)}$ vaterite (π-LBO) | LuBO$_3$ vaterite (π-LBO) | Lu$^{11}$BO$_3$ calcite (β-LBO) |
| molar mass (g/mol) | 221.94 | 233.78 | 233.78 |
| space group | monoclinic, *C*2/*c* (No. 15) | hexagonal, *P*6$_3$/*mmc* (No. 194) | trigonal, *R*$\bar{3}$*c* (No. 167) |
| lattice constants | | | |
| *a* (Å) | 11.173(4) | | |
| *b* (Å) | 6.461(21) | 3.727 | 4.914(13) |
| *c* (Å) | 9.462(30) | 8.722 | 16.21(7) |
| β (deg) | 112.763(15) | | |
| cell volume (Å$^3$) | 629.93(5) | 104.92 | 339.05(2) |
| *Z* | 12 | 2 | 6 |
| calcd density, (g/cm$^3$) | 7.343 | 7.42 | 6.871 |
| ref | this work | 11 | this work |

The coexistence of the BO$_3$ and BO$_4$ units in π-LBO can be further demonstrated by FT-IR, which is one of the most efficient methods to distinguish the difference of the bonds. Figure 8 shows the FT-IR of π- and β-LBO in the wavenumber range of 500–2000 cm$^{-1}$; their corresponding vibration modes are tabulated in Table S4 in the SI. Both the planar triangle and tetrahedral unit have been studied many times, and the expected locations of the bands can be inferred from ref 16. At room temperature, the β-LBO phase presents seven peaks located at 627, 719, 735, 769, 1170, 1230, and 1408 cm$^{-1}$, while the π-LBO phase exhibits seven peaks at about 573, 719, 870, 930, 1014, 1068, and 1408 cm$^{-1}$. In the β-LBO phase, 1170, 1230, and 1408 cm$^{-1}$ in the high-frequency range can be assigned to the antisymmetric stretching of the B–O bond of the trigonal BO$_3$ units. In addition, in the low-frequency range, 627, 719, 735, and 769 cm$^{-1}$ in the β-LBO phase belong to the BO$_3$ bending. For the π-LBO phase, the corresponding vibration peaks of the BO$_3$ units (1408 and 719 cm$^{-1}$) and BO$_4$ units (573, 870, 930, 1014, and 1068 cm$^{-1}$) could be identified. 1014 and 1068 cm$^{-1}$ in the π-LBO phase could be attributed to the stretching relaxation of the tetrahedral BO$_4$ units, and 573, 870, and 930 cm$^{-1}$ in the π-LBO phase could be assigned to the B–O–B bending and borate ring deformation.[16,17] Thus, the existence of an open B$_3$O$_9$ ring consisting of BO$_3$ and BO$_4$ units in the π-LBO phase can be demonstrated by the FT-IR results.

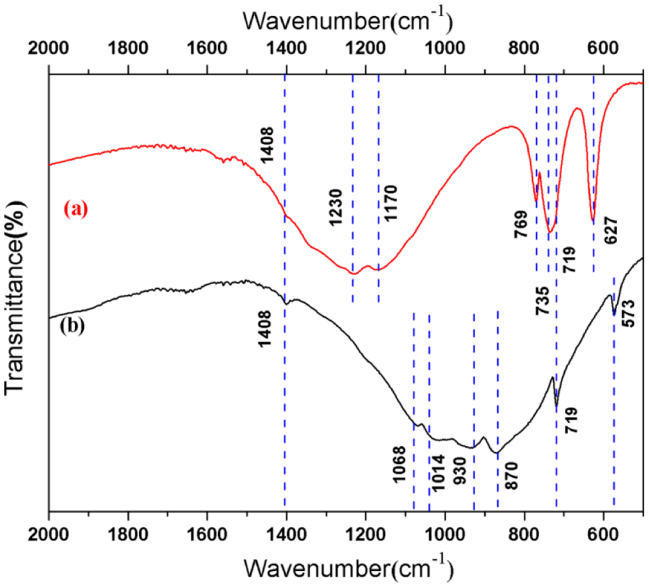

**Figure 8.** FT-IR spectra of β-LBO (a) and π-LBO (b).

### 3.2. Photoluminescence Properties of Ce$^{3+}$ in π- and β-LBO.

The emission and excitation spectra of Ce$^{3+}$ in π- and β-LBO are presented in Figure 9. Under 366 nm excitation, Ce$^{3+}$-activated π-LBO displays obviously doublet emission bands in the wavelength range of 375–500 nm with the peak centers at about 393 and 423 nm, respectively (Figure 9d). For comparison, we can see that Ce$^{3+}$-activated β-LBO can be efficiently excited under 337 nm, introducing a broad emission band with a peak at 363 nm together with a shoulder at about 397 nm. These two broad emission bands for Ce$^{3+}$ in π- and β-LBO can be well decomposed into two Gaussian components, respectively. It is believed that these two emission sub-bands are the characteristic splitting of the emission bands of Ce$^{3+}$ due to the spin–orbit splitting of the ground state. These bands should correspond to the 5d → $^2F_J$ ($J = {}^7/_2, {}^5/_2$) transitions of Ce$^{3+}$. The $F_J$ ($J = {}^7/_2, {}^5/_2$) energy gaps of Ce$^{3+}$ in π- and β-LBO are 1850 and 2350 cm$^{-1}$, respectively, which are very close to the $F_J$ ($J = {}^7/_2, {}^5/_2$) energy gap of Ce$^{3+}$ (2000 cm$^{-1}$) in most Ce$^{3+}$-activated phosphors.[18] Moreover, π-LBO:Ce$^{3+}$ exhibits emission properties similar to those of Ce$^{3+}$ with almost the same shape profiles and peak positions when under VUV photons at 158 nm or UV photons at 249 nm (see Figure 3 in the SI). There is one principle excitation band in the excitation spectra of π-LBO:Ce$^{3+}$ located in the wavelength range of 300–390 nm with the peak centered at 366 nm, regardless of the monitoring wavelength (Figure 9c). In addition, a small shoulder at 343 nm and a weak excitation peak at about 242 nm are observed, which is in good agreement with the observation in the VUV excitation spectra of π-LBO:Ce$^{3+}$ by monitoring the emission bands at 393 and 420 nm. The broad band with a maximum at 158 nm in the VUV region is considered to be the host absorption band, and the other two peaks at 219 and 240 nm are attributed to the 4f–5d transitions

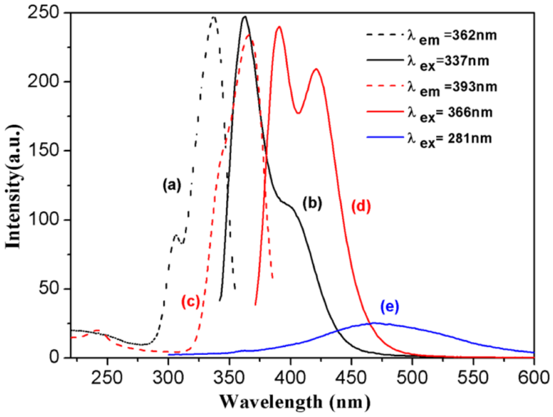

**Figure 9.** Excitation and emission spectra of LBO:Ce$^{3+}$ at room temperature compared to BGO under the same conditions: (a) excitation spectrum of β-LBO:Ce$^{3+}$ (1 mol %) monitored at 362 nm; (b) emission spectrum of β-LBO:Ce$^{3+}$ (1 mol %) under 337 nm; (c) excitation spectrum of π-LBO:Ce$^{3+}$ (1 mol %) monitored at 393 nm; (d) emission spectrum of π-LBO:Ce$^{3+}$ (1 mol %) under 366 nm; (e)emission spectrum of the BGO powder under 281 nm.

of $Ce^{3+}$ (see Figure S3 in the SI). Thus, the excitation bands at 198, 221, 241, 343, and 366 nm are assigned to the transition from the $^2F_{5/2}$ ground state of $Ce^{3+}$ in $\pi$-LBO to the excited levels of the 5d configuration split by the crystal-field interactions. A broad excitation band with a peak at 337 nm and a shoulder at 305 nm was observed for $\beta$-LBO:$Ce^{3+}$ by monitoring the emission band at 362 nm. It is worth noting that both $\pi$- and $\beta$-LBO:$Ce^{3+}$ exhibit similar emission and excitation bands; more importantly, the integral area of the emission bands is about 4 times that of BGO under the same measurement conditions. Table 3 summarizes the luminescence properties of $Ce^{3+}$ in $\pi$- and $\beta$-LBO for comparison.

**Table 3. Luminescence Properties of $Ce^{3+}$ in $\pi$- and $\beta$-LBO at Room Temperature**

| luminescence properties | $\pi$-LBO | $\beta$-LBO |
|---|---|---|
| excitation bands (nm) | 198, 221, 241, 343, 366 | 305, 337 |
| emission band maximum (nm) | 393, 423 | 363, 397 |
| $D(Ce^{3+}, A)$ ($cm^{-1}$) | 22020 | 19670 |
| Stokes shift ($cm^{-1}$) | 1870 | 2120 |
| decay time $\tau$ (ns) | 33 | 20 |
| ref | this work | this work, 8 |

It is well-known that the relative energy of the first f−d transition for different $RE^{3+}$ ions is almost independent of the host, and the 5d level of $RE^{3+}$ ions in the defined crystal shows somewhat lower energies compared with the 5d orbital energy of the free $RE^{3+}$ ions. Therefore, it is easy to predict that the decrease of the 5d energy for the different $RE^{3+}$ ions in a similar lattice must exhibit some relationship. Dorenbos provided the 4f−5d transition energies of triply ionized lanthanides in various compounds and proposed that the crystal-field decrease $D(Ln,A)$ for the energy of the $4f^{n-1}5d$ levels of a lanthanide ion in compound A relative to the same level energies in the free ion, i.e.

$$D(\mathrm{Ln, A}) = E(\mathrm{Ln, free}) - E(\mathrm{Ln, A}) \tag{1}$$

is almost independent of the nature of the lanthanide ion doped.

Here, $E(Ln,free)$ is the energy of the first f−d transition of $Ce^{3+}$ as free (gaseous) ions. $E(Ln,A)$ is the f−d energy difference of the lanthanide ions $Ln^{3+}$ doped in compound A. The lowest 4f−5d excitation transitions of $Ce^{3+}$, $E(Ce^{3+},\pi\text{-LBO})$ and $E(Ce^{3+},\beta\text{-LBO})$, were found to be 366 nm (i.e., 27320 $cm^{-1}$) and 337 nm (i.e., 29670 $cm^{-1}$), respectively. The 5d level of free $Ce^{3+}$ was 49340 $cm^{-1}$.[19] Therefore, the f−d transitions energy of $Ce^{3+}$ in $\pi$- and $\beta$-LBO was decreased by 22020 and 19670 $cm^{-1}$, respectively, compared with that of free $Ce^{3+}$ ion. It is implied that $D(Ce^{3+},\pi\text{-LBO})$ and $D(Ce^{3+},\beta\text{-LBO})$ were 22020 and 19670 $cm^{-1}$, respectively.

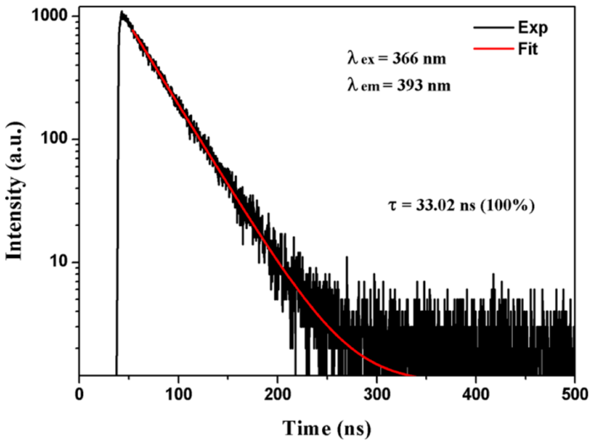

**Figure 10.** Fluorescence decay curve of $\pi$-LBO:$Ce^{3+}$ (1 mol %) at room temperature.

The fluorescence decay curve of $\pi$-LBO:$Ce^{3+}$ (1 mol %) under UV excitation is illustrated in Figure 10, together with the single-exponential decay fit curve. The monitoring excitation and emission wavelengths were fixed at the effective 4f−5d transitions of $Ce^{3+}$ (i.e., $\lambda_{ex}$ = 366 nm and $\lambda_{em}$ = 393 nm), respectively. The solid curve of the sample in the interval from 20 to 300 ns can be well fitted with a single-exponential decay $I(t) = I_0 \exp(-t/\tau)$, where $I_0$ is the initial spectral intensity and $\tau$ is the decay time constant of the emission. The decay time of $Ce^{3+}$ in $\pi$-LBO is about 33 ns, which features the typical decay time value of $Ce^{3+}$ 5d−4f emission in many other host lattices.[20,21] The decay time of $Ce^{3+}$ in $\pi$-LBO is a little slower than that of $\beta$-LBO (about 20 ns).[8] It is worth noting that two different Lu sites in the $\pi$-LBO crystal structure will lead to the two exponential terms as expected. However, only a single-exponential term was observed, probably because of the fact that the coordination environments for both Lu sites are too similar to be distinguished. The Stokes shift of $Ce^{3+}$ in these two host lattices was estimated from the energy difference between the lowest 5d excitation level and the first emission band at high energy by the decomposed $Ce^{3+}$ excitation and emission spectra. The Stokes shift of $Ce^{3+}$ in $\pi$-LBO is smaller than that in $\beta$-LBO, which is in contrast with the value of the crystal-field decrease $D(Ce^{3+},A)$ discussed previously. The detailed luminescence mechanisms of $Ce^{3+}$ in $\pi$- and $\beta$-LBO are shown in Figure S4 in the SI, which show the influences, namely, the centroid shift, crystal-field splitting (CFS), and Stokes shift from the host lattice on $Ce^{3+}$. The centroid shift ($\varepsilon_c$) of the bonding is commonly associated with the nephelauxetic effect, which is often attributed to the covalency between the $Ce^{3+}$ 5d orbital and the p orbitals of the anions.[22] Because of the same types of cation (Lu), anion (O), and activator (Ce), the centroid shift ($\varepsilon_c$) of $Ce^{3+}$ should be similar in both $\pi$- and $\beta$-LBO. However, the CFS is mainly determined by the environment (e.g., coordination number, etc.) of the first anion coordination polyhedron, and there is no significant influence of the chemical properties and charge state of the anions on the CFS.[23] In our present work, it is difficult to observe all of the CFS of the $Ce^{3+}$ 5d levels, making it impossible to distinguish the separate effect of the nephelauxetic effect and CFS. Therefore, the crystal field decrease $D(Ln, A)$ was used to determine the combined effect of nephelauxetic effect and CFS. Because the centroid shift ($\varepsilon_c$) of $Ce^{3+}$ should be similar in both $\pi$- and $\beta$-LBO, the difference of the crystal-field decrease [$D(Ce^{3+},\pi\text{-LBO})$ = 22020 $cm^{-1}$ and $D(Ce^{3+},\beta\text{-LBO})$ = 19670 $cm^{-1}$] can be attributed to the difference of their CFS effect. As aforementioned, the coordination number of $Lu^{3+}$ in $\pi$-LBO (CN = 8; the average Ce−O bond is about 2.335 Å) is larger than that of $\beta$-LBO (CN = 6; the average Ce−O bond is about 2.241 Å), leading to the larger CFS effect in $\pi$-LBO. The Stokes shift ($\Delta S$) is related to the ease of relaxation of the excited ion in the lattice. It determines the difference between the emission and excitation energy, which is lost during the vibrational relaxation process. Generally, the Stokes shift tends to decrease in more rigid host lattices. The Stokes shift of $Ce^{3+}$ in $\pi$-LBO ($\Delta S$ = 1870 $cm^{-1}$) is smaller than that of $\beta$-LBO ($\Delta S$ = 2120 $cm^{-1}$), indicating that $\pi$-LBO exhibits more rigid host lattices than $\beta$-LBO.

## 4. CONCLUSIONS

The crystal structure of low-temperature vaterite $\pi$-LBO was investigated, using neutron diffraction patterns, FT-IR spectra, and HRTEM. It was demonstrated that the vacancy-stabilized low-temperature vaterite $\pi$-LBO can be obtained at high temperature. The existence of an open $B_3O_9$ ring consisting of $BO_3$ and $BO_4$ units in $\pi$-LBO introduced by the B and O vacancies was confirmed by FT-IR. Moreover, the luminescence properties and corresponding mechanism of $Ce^{3+}$ in $\pi$- and $\beta$-LBO were studied in detail. The investigation of the phase transition between $\pi$- and $\beta$-LBO not only paves the way for the large-size $\beta$-LBO single-crystal growth but also provides some new insight for the further understanding of the luminescence mechanism.

## ■ ASSOCIATED CONTENT

### Ⓢ Supporting Information

Rietveld-refined neutron powder diffraction pattern of $\beta$-$L^{11}BO$ at room temperature, projection of the crystal structure of $\beta$-LBO, VUV–UV excitation and emission spectra of $\pi$-LBO:$Ce^{3+}$ at room temperature under the same conditions, luminescence mechanism of $Ce^{3+}$ in $\pi$- and $\beta$-LBO, atom coordinates and isotropic equivalent displacement parameters for $\pi$- and $\beta$-$L^{11}BO$, selected bond distances and angles in the structure of $\pi$-$L^{11}BO$, and observed frequencies of the different vibration modes in $\pi$- and $\beta$-LBO. This material is available free of charge via the Internet at http://pubs.acs.org.

## ■ AUTHOR INFORMATION

### Corresponding Author

*E-mail: jtzhao@shu.edu.cn. Tel:+86-21-52412073

### Notes

The authors declare no competing financial interest.

## ■ ACKNOWLEDGMENTS

This work was supported by the National Natural Science Foundation of China under Grant 11104298, the U1332202 Innovation program of Shanghai Institute of Ceramics under Grant Y34ZC130G, and the Open Fund of Key Laboratory of Transparent Opto-functional Inorganic Materials, Shanghai Institute of Ceramics of Chinese Academy of Sciences. The authors thank Professor David Walker at Columbia University, New York, NY, for his help on the high-pressure work.

## ■ DEDICATION

Dedicated to the memory of Prof. J. D. Corbett.

## ■ REFERENCES

(1) Boyer, D.; Bertrand-Chadeyron, G.; Mahiou, R.; Caperaa, C.; Cousseins, J. C. *J. Mater. Chem.* **1999**, *9*, 211–214.

(2) Velchuri, R.; Kumar, B. V.; Devi, V. R.; Prasad, G.; Prakash, D. J.; Vithal, M. *Mater. Res. Bull.* **2011**, *46*, 1219–1226.

(3) Zhang, L.; Pedrini, C.; Madej, C.; Dujardin, C.; Gacon, J. C.; Moine, B.; Kamenskikh, I.; Belsky, A.; Shaw, D. A.; MacDonald, M. A.; Mesnard, P.; Fouassier, C.; Van't Spijker, J. C.; van Eijk, C. W. E. *Radiat. Eff. Defects Solids* **1999**, *150*, 47–52.

(4) Hatamoto, S. I.; Yamazaki, T.; Hasegawa, J.; Katsurayama, M.; Oshika, M.; Anzai, Y. *J. Cryst. Growth* **2009**, *311*, 530–533.

(5) Yanagida, T.; Fujimoto, Y.; Kawaguchi, N.; Yokota, Y.; Kamada, K.; Totsuka, D.; Hatamoto, S.-I.; Yoshikawa, A.; Chani, V. *Nucl. Instrum. Methods Phys. Res., Sect. A* **2011**, *652*, 251–255.

(6) Levin, E. M.; Roth, R. S.; Martin, J. B. *Am. Mineral.* **1961**, *46*, 1030–1055.

(7) Wu, Y. T.; Ding, D. Z.; Yang, F.; Pan, S. K.; Ren, G. H. *Mater. Res. Bull.* **2012**, *47*, 106–110.

(8) Wu, Y. T.; Ding, D. Z.; Pan, S. K.; Yang, F.; Ren, G. H. *J. Alloys Compd.* **2011**, *509*, 366–371.

(9) Lin, J. H.; Sheptyakov, D.; Wang, Y. X.; Allenspach, P. *Chem. Mater.* **2004**, *16*, 2418–2424.

(10) Larson, A. C.; Von Dreele, R. B. *Los Alamos Natl. Lab. Rep.* **1994**, 86–748.

(11) Pitscheider, A.; Kaindl, R.; Oeckler, O.; Huppertz, H. *J. Solid State Chem.* **2011**, *184*, 149–153.

(12) Bradley, W. F.; Graf, D. L.; Roth, R. S. *Acta Crystallogr.* **1966**, *20*, 283–287.

(13) Zhang, Z. J.; Zhang, H.; Duan, C. J.; Yuan, J. L.; Wang, X. J.; Xiong, D. B.; Chen, H. H.; Zhao, J. T. *J. Alloys Compd.* **2008**, *466*, 258–263.

(14) Shannon, R. D. *Acta. Crystallogr., Sect. A* **1967**, *32*, 751–767.

(15) Huppertz, H.; von der Eltz, B.; Hoffmann, R. D.; Piotrowski, H. *J. Solid State Chem.* **2002**, *166*, 203–212.

(16) Weir, C. E.; Schroeder, R. A. *J. Res. Natl. Bur. Stand.* **1964**, *68A*, 465–487.

(17) Weir, C. E.; Lippincott, E. R. *J. Res. Natl. Bur. Stand.* **1961**, *65A*, 173–183.

(18) Blasse, G.; Bril, A. *J. Chem. Phys.* **1967**, *47*, 5139–5145.

(19) Zhang, Z. J.; ten Kate, O. M.; Delsing, A.; van der Kolk, E.; Notten, P. H. L.; Dorenbos, P.; Zhao, J. T.; Hintzen, H. T. *J. Mater. Chem.* **2012**, *22*, 9813–9820.

(20) Zhang, Z. J.; Feng, A.; Sun, X. Y.; Guo, K.; Man, Z. Y.; Zhao, J. T. *J. Alloys Compd.* **2014**, *592*, 73–79.

(21) Yuan, J. L.; J, W.; Zhang, Z. J.; Zhao, J. T.; Zhang, G. B. *Opt. Mater.* **2008**, *30*, 1327–1334.

(22) Dorenbos, P. *Phys. Rev. B* **2000**, *62*, 15640–15649.

(23) Dorenbos, P. *Phys. Rev. B* **2001**, *64*, 125117~1–12.